

# **THERMODYNAMIC MODELLING TO SUPPORT PRODUCTION OF HIGH NITROGEN STEELS BY DIFFERENT PROCESSES**

F. Ruffini, O.Tassa, A. Carosi, F. Arcobello, B. Giambi

Centro Sviluppo Materiali, Via di Castel Romano 100, 00128 Roma, Italy

## **ABSTRACT**

High Nitrogen Stainless Steel (HNSS) have a high potential for several applications due to their attractive properties: by varying the range of composition of the steel, metallurgists are exploiting these materials for many important applications. Actually, there are some processing routes available: the most part of the world production of HNSS is made by electric plus AOD for low-medium content of N and by PESR for high content of nitrogen

The main criticality that can be encountered during the solidification of high nitrogen steels is the formation of gas bubbles due to supersaturation of nitrogen in the melt, that induces porosity in the final macrostructure. Therefore, tools for prediction of solidification behaviour of HNSS under different casting conditions, are required to prevent defectiveness due to pores in the final products. In the present work, a simple microsegregation model interfaced with Thermocalc has been implemented, which allows to predict the conditions for gas nucleation during solidification. This model has been validated by comparison with experimental results of solidification of different HNSS grades in conditions variable from vacuum to high pressure, and represents an useful tool to support HNSS industrial production.

**KEYWORDS:** High Nitrogen Stainless Steel, Microsegregation, Modelling, PESR, gas nucleation

## **INTRODUCTION**

Nitrogen alloyed stainless steels, both austenitic and martensitic, exhibit attractive properties such as high strength and ductility, good corrosion resistance and reduced tendency to grain boundary sensitisation. Furthermore nickel saving reduces costs for austenitic steels[1-4].

The melting of high nitrogen steels (HNSS) poses two problems: how to get high nitrogen contents into the melt and how to keep it in solution during the process of solidification. Gas porosity formation takes place in the solidification stage because of the low solubility limit of nitrogen into the ferrite phase: as a consequence, the liquid is strongly enriched in nitrogen.

There are two possible ways to overcome the low solubility of nitrogen in molten iron and to achieve a high nitrogen content in the steel: alloying with elements which lower the nitrogen activity or melting under pressure.

For this reason the development of the pressure electroslag remelting (PESR) is becoming a predominant interest for the production of steels having nitrogen content largely above the solubility limit under atmospheric pressure.

In the same time the need to develop models to evaluate the nitrogen limit content as function of composition and pressure is also increasing, in order to supply a tool able to tune pressure as function of steel composition.

Aim of this paper is to describe the work performed to develop a model able to treat the different aspects related to the solidification of HNSS. To evaluate the microsegregation, a code, linked to Thermocalc model has been developed, which permits to calculate the nitrogen enrichment in the residual melt as a function of pressure, composition and solidification rates. As a matter of fact, this code allows to determine at which solidification stage the gas pore nucleation occurs.

# 1. MODEL DESCRIPTION

In the present work, a simple uni-dimensional microsegregation model has been implemented, in order to evaluate the possibility of gas nucleation during solidification of high nitrogen steels, in different pressure conditions.

In the model, microsegregation in multicomponent systems has been evaluated coupling the classical model developed by Cline-Kurz [5] with Thermocalc [6-7], a software and a thermodynamic database for the prediction of equilibria in multicomponent systems. In this way, it has been possible to take in account the effect of pressure on solubility limits in the liquid phase and to evaluate the partition coefficients between liquid and solid for each solute element, as a function of temperature and concentrations.

Generally, during solidification a rejection of solutes at the liquid/solid interface toward the liquid phase occurs when the solubility of the solute elements in the solid is smaller than that in the liquid. At the same time, a certain level of back-diffusion in the solute phase takes place, as an effect of the increase of solute concentration at the interface and therefore of the associated gradient in the solid. This phenomenon can be modelled by considering a small volume element of the mushy zone, as represented in fig.1.

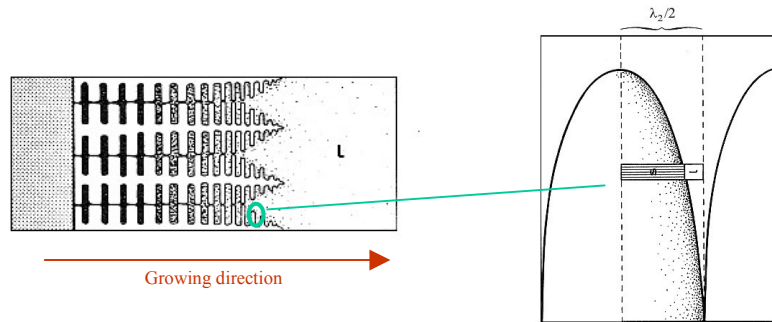


Fig. 1. Volume element of the mushy zone considered in the model

In the hypothesis of thermodynamic equilibrium at the liquid/solid interface, solute redistribution between the two phases can be described by the Brody and Flemings model [8], which assumes complete diffusion in the liquid phase and incomplete back-diffusion in the solid phase.

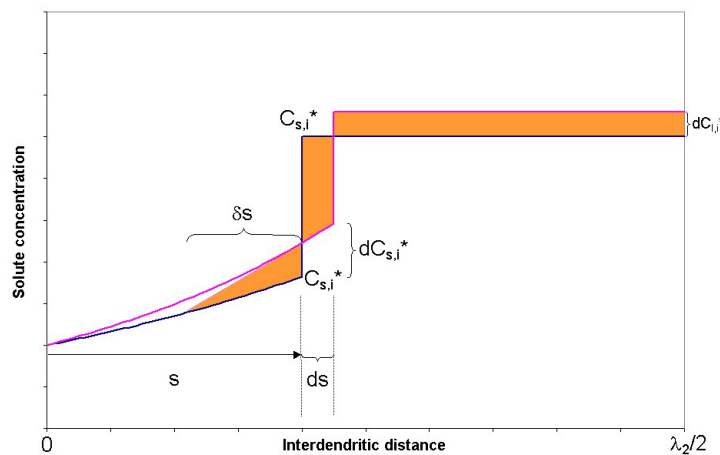


Fig.2. Solute redistribution at solid/liquid interface

The mass balance for the unit area during the interface advancement (see fig.2), considering the generic solute, can be written as follows:

$$(C_{l,i} - C_{s,i}^*) ds = \left( \frac{\lambda_2}{2} - s \right) dC_{l,i}^* + dC_{s,i}^* \frac{\delta s}{2} \quad (1)$$

In relationship (1),  $C_{l,i}$  represents the uniform liquid concentration of the generic solute,  $C_{s,i}^*$  is the solute concentration at the interface,  $ds$  is the infinitesimal displacement of the interface,  $s$  is the solidified length,  $\delta s$  is the diffusion boundary layer in the solid phase,  $\frac{\lambda_2}{2}$  is the dimension of the volume element, equal to half the secondary dendrite arm spacing, and  $dC_{l,i}^*$  and  $dC_{s,i}^*$  are the solute concentration increases, respectively, in the residual melt and in the solid at the interface. The last term at the right hand side of relationship (1) is derived by a first-order approximation of diffusion in the solid.

The following terms can be introduced:

$$f_s = \frac{s}{\lambda_2/2}; \quad \delta s = 2D_{s,i} \frac{dt}{ds}; \quad C_{s,i}^* = k_i C_{l,i}^* \quad (2)$$

where  $f_s$  is the solid fraction,  $dt$  is the infinitesimal time necessary for the interface displacement,  $D_{s,i}$  and  $k_i$  are, respectively, the diffusion coefficient and the partition coefficient between solid and liquid for the generic solute in the solid phase.

Supposing that solidification proceeds according to a parabolic law with respect to the total solidification time  $t_f$ , relationship (1) can be therefore re-arranged as:

$$dC_{l,i}^* = \frac{df_s (1 - k_i) C_{l,i}^*}{(1 - f_s) + 2\alpha_i k_i f_s} \quad (3)$$

In the relationship (3), the dimensionless  $\alpha_i$  term has been defined as follows:

$$\alpha_i = \frac{4D_{s,i} t_f}{\lambda_2^2} \quad (4)$$

The parameter  $\alpha_i$  can be interpreted as the Fourier number of back-diffusion in the solid-state for the generic solute element, given by the ratio of the solidification time  $t_f$ , to the time for diffusion

in the solid state  $\left( \frac{\lambda_2^2}{4D_{s,i}} \right)$ . If diffusion in the solid is very fast (as for interstitial soluted elements),

the boundary layer  $\delta s$  is very large and the  $\alpha_i$  tends to infinity. In this case the relationship (3) is transformed into the ‘‘Lever-rule’’ model, which assumes complete diffusion of the element in both the liquid and the solid phases. The opposite limiting case is represented by the absence of diffusion in the solid phase; in this situation,  $\alpha_i$  tends to zero and relationship (3) becomes equal to the Scheil-equation [9].

Cline and Kurz proposed a modification of the Brody and Flemings model to ensure physical meaning, because relationship (3) does not assure mass conservation if the boundary layer  $\delta s$  is comparable to the solidified length  $s$ . They introduced a correction factor for  $\alpha_i$ , depending on its value, in order to limit the variability of the back-diffusion parameter. Therefore, a new parameter  $\alpha_i'$  was introduced, derived from  $\alpha_i$  as follows:

$$\alpha'_i = \alpha_i \left[ 1 - \exp\left(-\frac{1}{\alpha_i}\right) \right] - \frac{1}{2} \exp\left(-\frac{1}{2\alpha_i}\right) \quad (5)$$

According to relationship (5), when  $\alpha_i \rightarrow \infty$ ,  $\alpha'_i \rightarrow 0.5$  and when  $\alpha_i \rightarrow 0$ ,  $\alpha'_i \rightarrow \alpha_i$ .

The extension of this homogenisation process is ruled by  $\alpha'_i$ , which is a function of the diffusion coefficient in the solid state of each element, and depends on the cooling rate. This parameter, in fact affects both the distance  $\frac{\lambda_2}{2}$  over which the diffusion processes have to take place, and the solidification time. As a general trend, the higher the solidification time, the less effective is the back-diffusion processes, although diffusion distance is reduced.

In the present model, relationships (3) and (5) have been implemented in a numerical algorithm interfaced with Thermocalc software. Once defined the initial solute concentrations in the system, the phases involved in the solidification process and the local pressure (which includes both the atmospheric and the ferrostatic contributions) and the temperature step, the solidification pattern is determined by the iteration of the following sequence:

- at each temperature, the equilibrium between solid and liquid phases is evaluated by Thermocalc. The outputs of the calculation are the weight fractions of the phases and their compositions; on the basis of these values, all the parameters which appear in relationships (3) and (5) can be determined;
- in the second step, the effective build-up of each solute in the residual melt is evaluated by considering the back-diffusion process in the solid phase. The composition of remaining liquid is the input for the next temperature step. The solidified fraction is used for calculating the current solidified length  $s$ .

The sequence of the interface advancement/back-diffusion process is repeated until solidification process is completed. If nitrogen supersaturation is reached in the residual melt, a new gas phase will appear, with a depletion of the nitrogen content in the liquid. As solidification proceeds, the overall volume fraction of the gas phase is evaluated by cumulating its absolute fractions at each equilibrium.

In the described procedure, some aspects have been considered. First of all, in order to take into account the pressure effect on calculated equilibria, the SUB94 database has been “appended” to the FE-DATA one. In the second place, variable diffusion coefficients for different phases and temperatures have been considered, according to diffusion data reported by Miettinen for stainless steels, reported in tab.I [10]. Nucleation undercooling and fluid-flow effects were assumed negligible. Finally the following general relationship between cooling rates and secondary dendrite arm spacing has been adopted:

$$\lambda_2 = k\dot{T}^{-\alpha} \quad (6)$$

where  $\dot{T}$  is the cooling rate, and  $\alpha=0.45$  e  $k=68$ , according to Sugiyama [11] determinations for stainless steel.

Since the solidification time is a function of  $\alpha'_i$ , and this in turn depends on the solidification time through the relationship (4), once a suitable cooling rate for the considered solidification process has been defined, the described sequence is repeated until convergence is found between the supposed solidification time and the calculated one.

Tab.I. Diffusion constants and activation energies for the considered elements in the ferrite, austenite and liquid phases.

Element	Ferrite		Austenite		Liquid	
	$D_0$ ( $J/m^2 * 10^4$ )	Q (J/mol)	$D_0$ ( $J/m^2 * 10^4$ )	Q (J/mol)	$D_0$ ( $J/m^2 * 10^4$ )	Q (J/mol)
C	0.013	81400	0.96	171500	7.67E-02	100600
Ni	1.6	240000	0.2	272000	1.30E-02	89200
Cr	1.5	229700	0.077	251000	2.51E-03	66900
Cu	2.6	240000	0.7	286000	5.30E-05	0
Si	8	248900	0.3	260000	5.10E-04	38300
N	0.008	79100	0.91	168500	9.76E-03	72800
Mn	0.76	224400	0.412	264000	4.60E-03	70300
Mo	3.47	241400	0.068	246900	5.82E-04	41800

## 2. EXPERIMENTAL PROCEDURE

In order to verify the reliability of the model in the prediction of solidification behaviour of high nitrogen steels, some casting trials have been performed by different processes. Three ingots (about 10 kg) of austenitic stainless steels have been cast on a laboratory scale using a HF induction furnace under argon atmosphere at 0.9bar. Nitrogen and manganese contents have been varied to realize compositions with different susceptibility to gas bubble formation during solidification; in particular the manganese content has been varied, since this element has a strong influence on nitrogen solubility. Then, another ingot of a ferritic stainless steel (about 50 kg) has been cast on a IM (Induction Melting) furnace under nitrogen atmosphere at 0.35bar.

Finally, an ingot of high nitrogen martensitic stainless steel has been re-melted in a PESR device. This process is adopted in the production of high nitrogen steels because it couples the material transfer between liquid metal and liquid slag, in order to nitride the re-melted steel, with the high pressure of the surrounding atmosphere, which allows to increase the nitrogen solubility limit in the liquid. In the present activities the nitriding have been made at CSM by Pressurised Electro Slag Remelting furnace.

Composition ranges of various ingots and the relative casting pressure are reported in tab.II. Ingots' sections have been realized along different directions (longitudinal or transversal) and examinations have been made to verify the presence of gas pores in the macrostructure.

Tab.II. Spectrum of indicative compositions and process conditions

Ingot	C	Ni	Cr	Cu	Si	N	Mn	Mo	Steel grade	Casting condition
A	0.100	3.11	18.56	1.95	0.43	0.41	11.27	0.01	Austenitic	HF at 1bar
B	0.093	3.12	18.73	1.91	0.40	0.40	7.91	0.01		
C	0.090	3.03	18.13	1.95	0.42	0.40	4.3	0.01		
D	0.06-0.10	0.4-0.5	13-15	-	0.4-0.8	0.10-0.20	0.4-0.6	1-2	Ferritic	IM at 0.35bar
E	0.2-0.3	0.4-0.8	13-15	-	0.4-0.8	0.2-0.4	0.4-0.6	1-2	Martensitic	PESR at 70bar

## 3. EXPERIMENTAL RESULTS

Longitudinal sections of HF ingots are reported in fig.3; it is clearly visible a significant difference in their macrostructure. No porosity due to gas nucleation can be recognized in the ingot A, and the presence of cavities due to solidification shrinkage has been found in the upper part of the ingot

only. Ingot B reveals the presence of pores, mainly distributed in the inner and upper part of the ingot. Ingot C is interested by large and diffuse porosity, which affects the whole macrostructure.



Fig.3. Macrostructure of ingots produced by HF at 0.9 bar

Transverse section of IM ingot corresponding to alloy D, cut 20 mm below the top surface, is reported in fig.4. In this part of the ingot, the presence of large pores with diameters up to 2mm is clearly visible; Porosity has not been found in further sections at higher distances from the top surface.

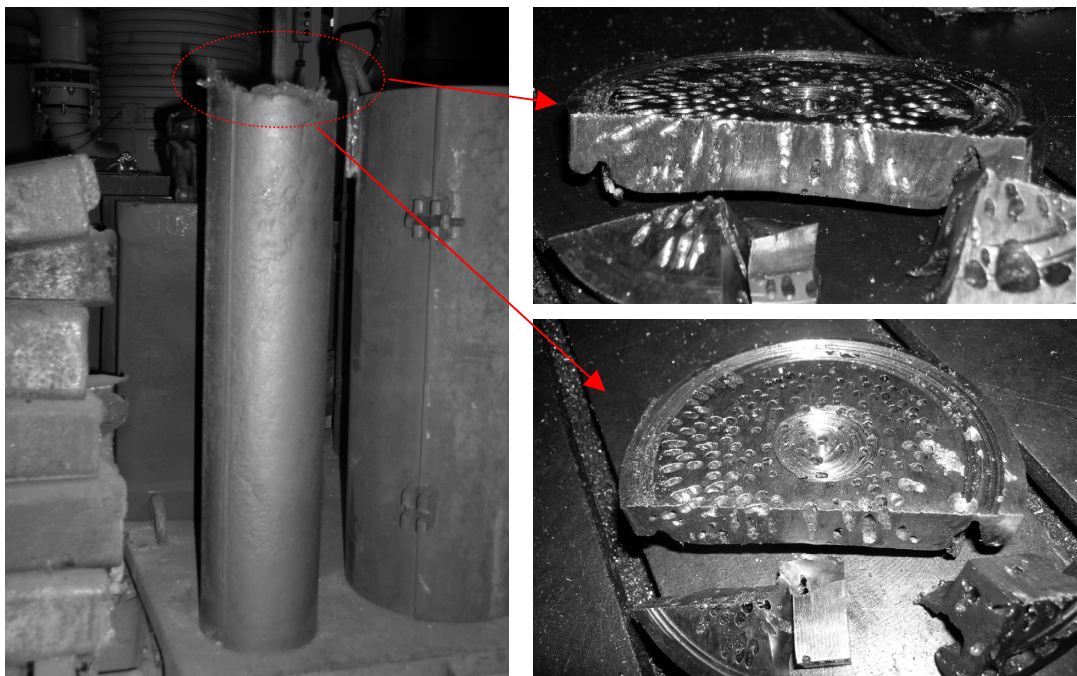


Fig.4. Porosity in the ingot “D” produced by IM process at 0.35 bar

The longitudinal section of PESR ingot (alloy E), illustrated in fig.5, does not show porosity. This reveals the effectiveness of PESR process to nitride alloys up to nitrogen contents above the solubility limit at atmospheric pressure.



Fig.5. Transversal section of the ingot “E” produced by PESR process at 70 bar

#### 4. DISCUSSION

In order to attempt an analysis of the obtained results, the model has been applied to the different experimental conditions, and the outputs have been compared with calculations from thermodynamic models at equilibrium.

##### 4.1. INDUCTION FURNACE

In tab.III, thermodynamic predictions of solidification pattern at equilibrium for the compositions of ingots A, B, C, made by Thermocalc and FE-DATA database, are reported.

Tab.III. Predicted solidification pattern at equilibrium of composition casted in the HF furnace

Ingot	Solidification pattern	$T_{liq}$ (°C)	$T_{aus}$ (°C)	$T_{sol}$ (°C)
A	$L \rightarrow L+\delta \rightarrow L+\delta+\gamma \rightarrow \delta+\gamma \rightarrow \gamma$	1388.70	1373.60 (22.23% $\delta$ )	1331.83 (2.67% $\delta$ )
B	$L+gas \rightarrow L \rightarrow L+\delta \rightarrow L+\delta+gas \rightarrow$ $L+\delta+\gamma+gas \rightarrow L+\delta+\gamma \rightarrow \delta+\gamma \rightarrow \gamma$	1405.99	1378.47 (51.58% $\delta$ )	1350.35 (8.69% $\delta$ )
C	$L+gas \rightarrow L+\delta+gas \rightarrow L+\delta+\gamma+gas \rightarrow$ $\delta+\gamma+gas \rightarrow \gamma+gas \rightarrow \gamma$	1430.31	1388.17 (73.67% $\delta$ )	1370.49 (36.87% $\delta$ )

According to these calculations, all the alloys solidify as primary ferrite, with the subsequent formation of austenite by peritectic reaction. The gas formation is excluded only for composition A, corresponding to the highest manganese content, meanwhile the condition for gas nucleation condition is largely exceeded for the alloy C. For the alloy B, with an intermediate manganese amount, the condition for gas nucleation is reached only during solidification, as a consequence of the nitrogen enrichment in the residual melt, due to its partitioning with the ferritic phase; at the end of solidification, the gas phase is then predicted to disappear. This situation is graphically represented in fig.6, where the nitrogen solubility limit for the average of compositions of ingots A, B, C, is superimposed to the position of each alloy in the N-Mn domain. The position of the different points, with respect to the solubility limit, is indicative of the presence of gas phase at the beginning of solidification; alloy B is situated just on the boundary limit, thus revealing the tendency of this composition to form gas bubbles during solidification.

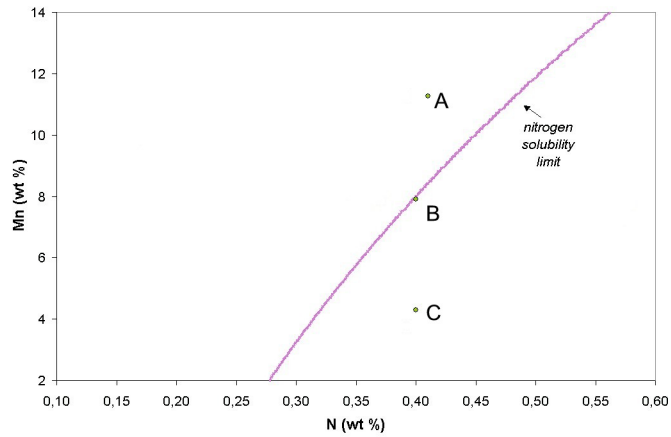


Fig.6. Nitrogen solubility limit at the beginning of solidification for alloys A,B,C at 0.9bar

In applying the microsegregation model a temperature step of 1K and cooling rate of 0.1K/s have been selected. The latter is a typical value for conventional continuous casting processes. Results of calculations are reported in fig.7, where the liquid and gas fractions are reported as a function of temperature. In fig.8, the nitrogen content in the residual melt during is plotted versus temperature.

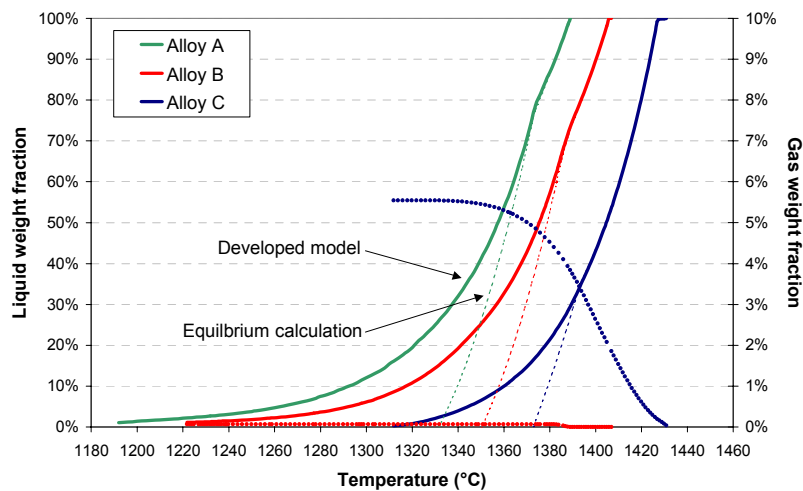


Fig.7. Predicted gas phase evolution during solidification of A,B,C alloys at 0.9bar

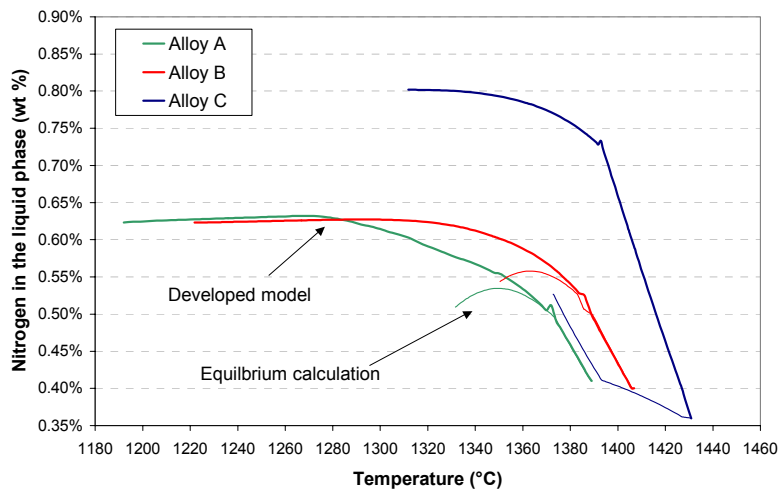


Fig.8. Predicted nitrogen pile-up in the residual melt during solidification of A,B,C alloys at 0.9bar

It can be observed that the model predictions are in agreement with the experimental results, whereas the equilibrium calculations give only a qualitative representation of the experiments.

In alloy A, the condition for gas phase nucleation is not predicted by the model during solidification, coherently with the absence of gas pores in the ingot microstructure. The main effect of nitrogen pile-up in the residual melt is the widening of the solidification temperature interval with respect to equilibrium calculations. The change of slope in the plotted curves is due to the peritectic reaction, which determines a modification of back-diffusion behaviour, due to the presence of a different phase at the interface with the liquid. For alloys C, the solidification path is characterized by the most intense nitrogen partition. This can be explained considering the low manganese content in the steel composition which produces a low solubility limit in the ferritic phase. The gas phase is always present during the whole solidification and it reaches a considerable fraction at the end of the process. This is in accordance with the evidence of large pores distributed all over the macrostructure of the ingot.

The behaviour of alloy B is the most interesting one. As predicted at equilibrium, the gas phase nucleates only at a certain stage of the solidification, as an effect of nitrogen partitioning from the primary ferritic phase. In the model, gas phase appears when the liquid fraction is equal to 0.7, before the beginning of the peritectic reaction. Since the nitrogen partitioning from the austenite to the liquid is less more effective, during the reaction  $L+\delta\rightarrow\gamma$  the gas phase growth is quite limited, as demonstrated by the calculated value of the cumulative gas fraction at the end of solidification, lower than 0.1%. Therefore it can be observed that the condition for gas phase nucleation is restricted to a small part of the solidification pattern, thus representing an effective limit for pores formation and growth. Moreover other physical limitations have to be considered. When the ferrostatic pressure is significant, as in the bottom part of the ingots, or when the interdendritic spaces are more narrow (typically in the superficial zones) the mechanical equilibrium for gas nucleation requires an high partial pressure of nitrogen, and consequently an elevated level of supersaturation. This can explain why the pores in ingot B appear localized in the inner and upper part of the ingot. These are the only regions where gas nucleation can take place in presence of a small driving force, since the ferrostatic pressure is minimal and the microstructure is coarser.

#### 4.2.IM PROCESS

The presence of pores in the ingot D was an unexpected problem occurred during the solidification process. Since the ingot was produced to be remelted as a consumable electrode in a further PESR stage, the presence of pores represented an unwanted feature, because it could compromise the welding of the electrodes and destabilize the remelting process. The choice of nitrogen content in the steel processed by IM was made in order to minimize its addition during the PESR process. Thus, a content lower than the solubility limit at 1550°C, the temperature at which the charge was melted in the furnace has been selected.

The behaviour of alloy D can be explained by evaluating the microsegregation phenomena occurred during solidification in low-pressure conditions. By applying the model to the alloy D, with a cooling rate of 1K/s and a temperature step of 1K, it has been found that the alloy D solidifies as primary ferrite and therefore is not interested by peritectic reactions. During the solidification process, the nitrogen partitioning into the liquid determines the overcoming of the solubility limit and the set up of conditions for gas nucleation. The predicted nitrogen pile-up is shown in fig.9, where the evolution of the liquid phase fraction is also reported. In this case, the conditions for gas nucleation are reached at an early stage of the solidification process, and therefore gas bubbles can easily grow.

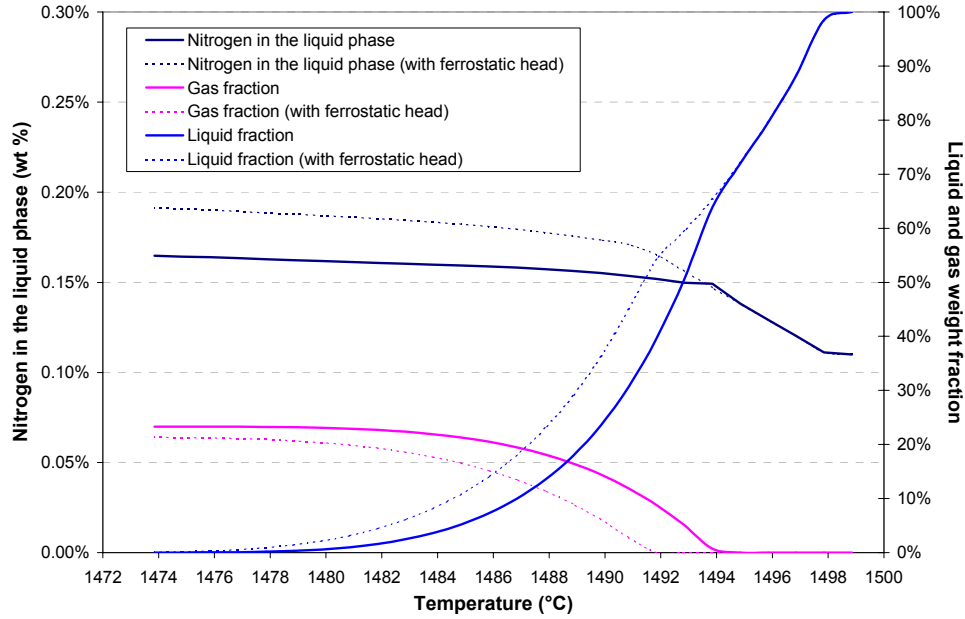


Fig.9. Predicted solidification behaviour of alloy D at 0.35 bar

As mentioned before, the contribution of ferrostatic head on liquid pressure, and the scale of dendritic structure which represents a physical limit to the gas bubble curvature, determine an increase of the nitrogen supersaturation in the liquid necessary for gas nucleation. Therefore, the effect of these two terms has been evaluated, adding the ferrostatic pressure, the pressure of 0.35bar inside the IM, and the pressure required by the formation of an interface between steel and gas. For a spherical bubble with curvature radius  $R$ , the latter is calculated as  $\Delta p_{\sigma} = 2\sigma_{s-g}/R$ , where  $\sigma_{s-g}$  is the liquid/gas interfacial energy. In fig.9, the dotted lines represent the solidification behaviour of alloy D in presence of a ferrostatic head of 2cm and a secondary dendrite arm spacing of  $70\mu\text{m}$ .

It is clearly visible that the nucleation conditions are reached at a lower temperature with respect to the previous calculation, which corresponds to an higher level of nitrogen content in the liquid phase. For instance, with a ferrostatic head of 0.5m, gas nucleation is predicted to shift to the last stages of solidification ( $f_l < 0.3$ ), where the surrounding solid phase can inhibit gas bubble coalescence and growth. This can justify the reason for the absence of porosity far from the top surface of the ingot.

Concluding, the implemented model has shown that nitrogen addition in IM process is quite dangerous for ingot integrity, because conditions for gas nucleation are easily reached during the solidification process. Therefore, if high nitrogen final contents are required, it would be a better choice to demand the great part of the nitriding process to the PESR stage.

#### 4.3. PESR PROCESS

The validation of the model for prediction of solidification in high pressure conditions is still in progress. The absence of porosity in the alloy E is predictable even with equilibrium calculations during solidification at 70bar. It is interesting to note that the microsegregation model could be useful to identify the proper operative pressure in PESR for each ingot to nitride. For alloy E, it can be predicted a value of 4bar as the threshold pressure to avoid thermodynamic conditions for gas nucleation. Therefore, it could be possible to carry on the nitriding process at a pressure far from the operative limit of the plant, which is desirable for the plant maintenance and safety.

## 5. CONCLUSIONS

In the present work, solidification of high nitrogen steel (HNSS) by different processes has been investigated. In particular the effect of pressure and composition on gas pore formation due to supersaturation of nitrogen in the liquid phase has been evaluated.

Since this aspect represents a severe problem for HNSS producers, a microsegregation model has been implemented in order to predict the evolution of liquid composition, and therefore the set up of conditions for gas phase nucleations, during the solidification process of high nitrogen steels. The model is interfaced with Thermocalc code and takes into account the effect of back-diffusion in the solid phase, which is treated separately for each solute; this phenomenon is particularly relevant for interstitial solute elements, like carbon and nitrogen, and should not be neglected in order to give reliable predictions of the microsegregation patterns. Moreover, other inputs of the model are the cooling rate and the pressure, which allow to compare conditions relative to different processes.

The model has been applied to different solidification processes of various HNSS grades, for pressure in the range from 0.35 up to 70bar. The model predictions, in terms of nitrogen pile-up in the liquid phase and gas phase formation, are in agreement with experimental results, and appear to be more accurate than those from equilibrium calculations.

The application of the model allowed to individuate the limitations in the solidification processes of different grades of HNSS at low pressures. On the other hand, a threshold value for the PESR process of a martensitic high nitrogen steel, without gas formation, has been individuated, which resulted lower than the operative limit of the plant.

The model can be applied as a useful tool to orient production of HNSS, since it is able to predict solidification conditions, and therefore the proper casting process, to prevent pore formation in the ingots. In addition, relevant indications on effective pressure requirements for PESR process can be evaluated, thus permitting a correct and protective use of the plant.

## REFERENCES

- 1) STEIN G., Int. J. Mater. Science and Product Technology 10, (1995); p.290.
- 2) BALACHANDRAN G. et al., ISIJ Int. 40, (2000), p.501.
- 3) UGGOWIDZER P. J., MAGDOWSKI R., SPEIDEL M. O., ISIJ Int. 36, (1996), p.901.
- 4) HOLZGRUBBER W., Proc. Int. Conf. on High Nitrogen Steels HNS – 88 (1989), p. 39.
- 5) T.W.CLYNE, W.KURZ, Metall. Trans. A, 12A (1981), p.965.
- 6) I.ANSARA, B.SUNDMAN, “The Scientific Group Thermodata groupe in Computer Handling and Dissemination of Data”, Ed. P S Glaser, Elsevier Science Publisher.
- 7) User’s Guide, Thermocalc.
- 8) H.D. BRODY, M.C. FLEMINGS, Trans. TMS-AIME, 236, (1996), p.615.
- 9) E. SCHEIL, Z.Metallkd, 34, (1942), p.70.
- 10) J.MIETTINEN, Metallurgical Transactions B, 28B, (1997), p.281.
- 10) SUGIYAMA et al., Tetsu to Haganè, 61, (1974), p.1094.